Optimization of photoluminescence of Y_2O_3:Eu and Gd_2O_3:Eu phosphors synthesized by thermolysis of 2,4-pentanedione complexes

2010 Nanotechnology 21 245702

(http://iopscience.iop.org/0957-4484/21/24/245702)

Nanotechnology **21** (2010) 245702 (7pp) doi:10.1088/0957-4484/21/24/245702

Optimization of photoluminescence of Y_2O_3:Eu and Gd_2O_3:Eu phosphors synthesized by thermolysis of 2,4-pentanedione complexes

B Antic[1,6], J Rogan[2], A Kremenovic[1], A S Nikolic[3], M Vucinic-Vasic[1], D K Bozanic[1], G F Goya[4] and Ph Colomban[5]

[1] Institute of Nuclear Sciences 'Vinca', POB 522, 11001 Belgrade, Serbia
[2] Faculty of Technology and Metallurgy, University of Belgrade, POB 494, 11000 Belgrade, Serbia
[3] Faculty of Chemistry, Department of Inorganic Chemistry, University of Belgrade, POB 158, 11001 Belgrade, Serbia
[4] Aragon Institute of Nanoscience and Condensed Matter Physics Department, University of Zaragoza, Zaragoza, Spain
[5] LADIR, UMR 7075 CNRS, and Université Pierre and Marie Curie (UPMC), 94230 Thiais, France

E-mail: bantic@vinca.rs

Received 11 February 2010, in final form 15 April 2010
Published 20 May 2010
Online at stacks.iop.org/Nano/21/245702

Abstract

Spherical shaped nanoparticles of series $Y_{2-x}Eu_xO_3$ ($x = 0.06$, 0.10, 0.20, and 2) and $Gd_{2-x}Eu_xO_3$ ($x = 0.06$, 0.10) were prepared by thermolysis of 2,4-pentanedione complexes of Y, Gd, and Eu. The bixbyite phase of $Gd_{2-x}Eu_xO_3$ samples was formed at 500 °C, whereas the thermal decomposition of Y and Eu complexes' mixtures occurred at higher temperatures. Linearity in the concentration dependence on lattice parameter confirmed the formation of solid solutions. The distribution of Eu^{3+} in $Gd_{2-x}Eu_xO_3$ was changed with thermal annealing: in the as-prepared sample ($x = 0.10$) the distribution was preferential at C_{3i} sites while in the annealed samples, Eu^{3+} were distributed at both C_2 and C_{3i} sites. Rietveld refinement of site occupancies as well as emission spectra showed a random distribution of cations in $Y_{2-x}Eu_xO_3$. The photoluminescence (PL) measurements of the sample showed red emission with the main peak at 614 nm ($^5D_0$–$^7F_2$). The PL intensity increased with increasing concentration of Eu^{3+} in both series. Infrared excitation was required to obtain good Raman spectra. The linear dependence of the main Raman peak wavenumber offers a non-destructive method for monitoring the substitution level and its homogeneity at the micron scale.

(Some figures in this article are in colour only in the electronic version)

1. Introduction

The oxides Y_2O_3 and Gd_2O_3 doped with Eu^{3+} (Y_2O_3:Eu and Gd_2O_3:Eu) are excellent red emitting phosphors with good thermal and chemical stability. They are used in plasma display panels (PDPs), field emission displays (FEDs), cathode ray tubes (CRTs), fluorescent lamps and laser devices, among others [1–3].

[6] Author to whom any correspondence should be addressed.

The production of phosphors for industrial applications requires chemical homogeneity, particle shape and size control, narrow particle size distribution, free of defects materials, etc. Both particle size and size distribution influence the luminescence. Spherically shaped particles have several advantages over other shapes. Their packing fraction is relatively high, forming a dense phosphor layer. Also, spherical particles minimize light scattering on the surface [2, 4]. For small particles there is a large

surface/volume ratio and, thus, a lot of active ions are on the surface. Because small particles have a large surface/volume ratio, a great number of active ions are on the surface. Since the crystal symmetry of the surface could be different compared to that of the particle core (and bulk counterpart), some new peaks in the luminescence spectra of nanoparticles were found [5]. For applications, narrow size distribution is advantageous and enables better formation of a uniform thickness of phosphor layer that affects uniform luminescence distribution across the whole phosphor screen [2, 4].

Microstructural and structural parameters that influence the luminescence (and other physical properties) strongly depend on preparation methods. There is a great number of papers considering various synthesis routes for rare earth oxide based phosphors. Some of these synthesis methods, such as mechanical alloying, induce an excess number of defects in structures. There is a challenge to apply new synthesis routes or to optimize existing ones with the aim of controlling microstructure and producing phosphors with enhanced luminescence. We have developed a method for synthesis of rare earth oxide based nanophosphors, by using thermal decomposition of acetylacetonato, 2,4-pentanedione, (AA) complexes. AA anion forms complexes with practically all metals, wherein both oxygen atoms bind to the metal to form a six-membered chelate ring. $[M(AA)_3]$ are soluble in organic solvents and have relatively low thermal decomposition temperatures, giving metal oxides as the main products and gases as the secondary one. The final result is as-prepared rare earth pure or mixed oxide with particle size ~5 nm with spherical morphology [6, 7].

The goal of this work was to apply a method based on thermolysis of $[M(AA)_3]$, M = Y, Eu, Gd to obtain $Y_{2-x}Eu_xO_3$ and $Gd_{2-x}Eu_xO_3$ nanopowders as well as to study the influence of Eu^{3+} concentration and thermal annealing on their vibration and photoluminescence (PL) properties.

2. Experimental details

2.1. Synthesis of Y_2O_3:Eu and Gd_2O_3:Eu

We used thermal decomposition of an appropriate mixture of coordination compounds containing acetylacetonato (AA = 2,4-pentanedionato) ligands ($[M(AA)_3]$, where M = Y, Eu, Gd) to synthesize $Y_{2-x}Eu_xO_3$ and $Gd_{2-x}Eu_xO_3$ nanopowders.

Preparation of complexes $[M(AA)_3]$, M = Y, Eu, Gd. $MCl_3{\cdot}6H_2O$, M = Y, Eu, Gd (0.1 mol), and NH_4AA (0.3 mol), freshly prepared by the reaction of 25% NH_3(aq) and AA, were suspended in 80 cm^3 of methanol. The mixture was refluxed for 60 min at 50 °C. Upon cooling for 24 h in a refrigerator and filtration, the precipitate was washed with cold water, recrystallized from toluene, and dried at 105 °C. All obtained complexes were light-yellow.

Preparation of $Y_{2-x}Eu_xO_3$ and $Gd_{2-x}Eu_xO_3$. To prepare the two sample series, $Y_{2-x}Eu_xO_3$ and $Gd_{2-x}Eu_xO_3$ (x = 0.06, 0.10, 0.20, and 2) complexes $[Y(AA)_3]$ and $[Eu(AA)_3]$, or $[Gd(AA)_3]$ and $[Eu(AA)_3]$, were milled and mixed in different molar ratios, and then heated in a furnace in air atmosphere at a heating rate of 10 °C min^{-1} up to 500 °C. The resulting products were kept at a final temperature for 10 min, and then cooled at 20 °C min^{-1} down to room temperature. The materials thus obtained were finally homogenized.

2.2. Experimental methods

2.2.1. Thermogravimetric (TGA) and differential thermal (DTA) analyses. The TGA and DTA analyses were performed simultaneously (30–1000 °C range) on an SDT Q600 TGA/DSC instrument (TA Instruments). The heating rates were 20 °C min^{-1} and the sample mass was less than 10 mg. The furnace atmosphere consisted of air at a flow rate of 100 cm^3 min^{-1}.

2.2.2. Raman spectroscopy. Three different instruments were used: (i) a high-resolution 'XY' spectrograph (Dilor, Lille, France) equipped with a double monochromator filter and a back-illuminated, liquid nitrogen cooled, 2000 pixels × 256 pixels CCD detector (Spex, Jobin-Yvon–Horiba Company); (ii) a high sensitivity multichannel notch-filtered INFINITY spectrograph (Jobin-Yvon–Horiba SAS, Longjumeau, France) equipped with a Peltier cooled CCD matrix used to record Raman spectra between 10 (XY instrument)/150 (INFINITY instrument) and 2000 cm^{-1}, using 488, 514.5, and 647.1 (XY)/532 and 632 nm (INFINITY) exciting lines (Ar^+–Kr^+/YAG, and He–Ne lasers), respectively (backscattering illumination and collection of the scattered light were made through an Olympus confocal microscope—long focus Olympus 10× or 50× objective, total magnification 100× and 500×, spot diameter ~100 and 10 μm in diameter); (iii) a Bruker RFS 100/S Fourier transform (FT) Raman spectrometer excited with a Nd-YAG 1064 μm laser diode and equipped with a liquid nitrogen cooled Ge detector. Spectra were recorded between 50 and 3500 cm^{-1} with a 4 cm^{-1} resolution or less. Both macro-(with a 90d collecting mirror, laser spot ~100 μm in diameter) and microsetting (40× near infrared (NIR) optimized objective, spot ~10 μm in diameter) are available.

2.2.3. Photoluminescence. The PL spectra were recorded using a Perkin-Elmer LS-3b fluorescence spectrophotometer at 390 nm excitation wavelength. For the emission measurements, the samples were prepared by casting the ethanol dispersion of nanopowders on glass plates and drying in air for 24 h.

2.2.4. Transmission electron microscopy (TEM) and x-ray powder diffraction data (XRPD). Particle size and shape were studied by TEM using a 200 keV JEOL-2000 FXII microscope. TEM samples were prepared by placing one drop of a dilute suspension of nanopowder in acetone, previously sonicated for 30 min, on a carbon coated copper grid. The solvent was allowed to evaporate slowly at room temperature. XRPD were collected on a PHILIPS PW 1710 automated x-ray powder diffractometer using Cu $K\alpha_{1,2}$ radiation. To refine

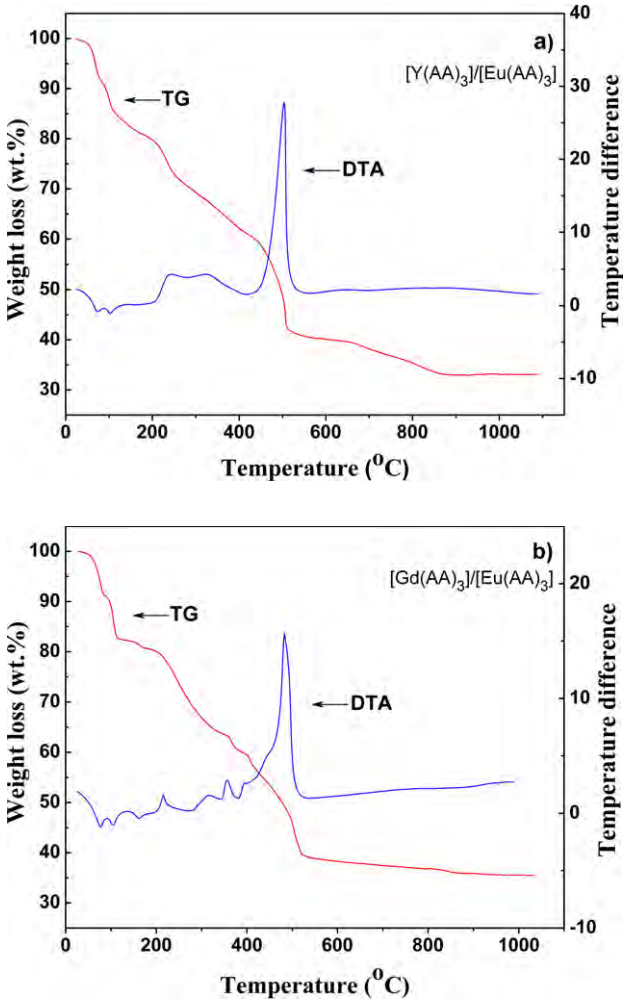

Figure 1. TGA and DTA of (a) $[Y(AA)_3]/[Eu(AA)_3]$ and (b) $[Gd(AA)_3]/[Eu(AA)_3]$.

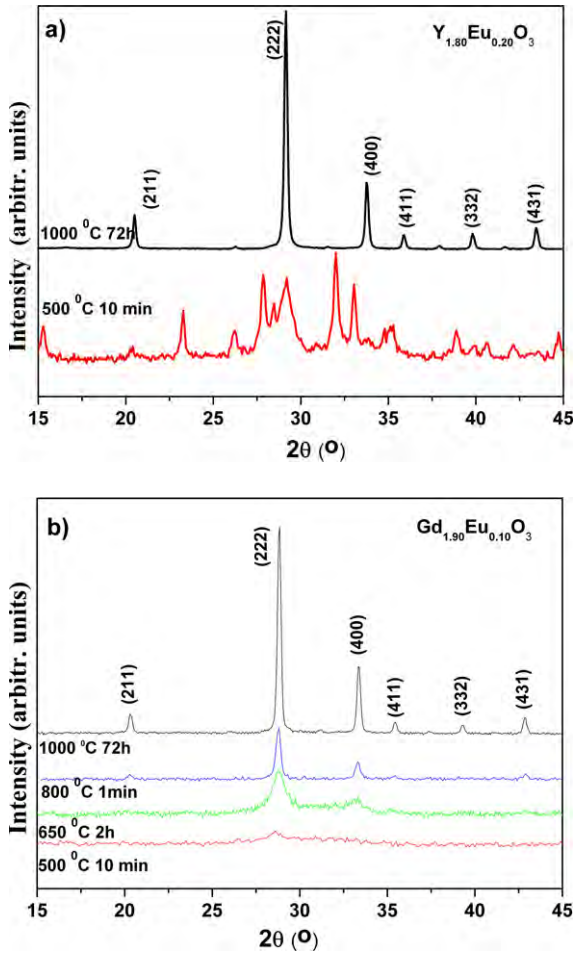

Figure 2. X-ray diffraction patterns of (a) $Y_{1.80}Eu_{0.20}O_3$ and (b) $Gd_{1.90}Eu_{0.10}O_3$ after thermal decomposition of $[M(AA)_3]$ complexes at 500 °C and after annealing at temperatures between 650 and 1000 °C (see text).

crystal structure, the data for an annealed $Y_{2-x}Eu_xO_3$ sample at 1000 °C were collected in steps of 0.05° in the angular range of 2θ between 15° and 115°. The counting time was fixed to 35 s at every step.

3. Results and discussion

3.1. TGA/DTA of sample formation

In order to control the synthesis process of the $Y_{2-x}Eu_xO_3$ and $Gd_{2-x}Eu_xO_3$ nanopowders, simultaneous TGA and DTA were performed (30–1000 °C ranges). The TGA and DTA curves of precursors $[Y(AA)_3]/[Eu(AA)_3]$ (**1**) and $[Gd(AA)_3]/[Eu(AA)_3]$ (**2**) that correspond to samples $Y_{1.80}Eu_{0.20}O_3$ and $Gd_{1.90}Eu_{0.10}O_3$ are presented in figures 1(a) and (b), respectively. XRPD patterns of $Y_{1.80}Eu_{0.20}O_3$ (after annealing at 500 and 1000 °C) and $Gd_{1.90}Eu_{0.10}O_3$ (after annealing at 500, 650, 800, and 1000 °C) are presented in figures 2(a) and (b), respectively.

Generally, the TGA and DTA curves are very similar for both complexing agents. The DTA curve for **1** (figure 1(a)) shows two endothermic peaks at 72 and 102 °C and three exothermic peaks at 239, 331, and 504 °C. The DTA curve for **2** (figure 1(b)) is very similar with three endothermic peaks at 80, 110, and 169 °C and four exothermic peaks at 225, 328, 372, and 505 °C. The endothermic DTA peaks for **1** and **2** are due to desolvation and evolution of the main fraction of the complexing agents up to about 180 °C with a weight loss of about 19% found for both compounds.

Further steps of thermal decomposition for **1** and **2** appear to be part of a very complex process. The decomposition of **1** is a three step process (figure 1(a)): up to 314 °C (weight loss found 32%), up to 412 °C (weight loss found 39%), and up to 573 °C (weight loss found 60%). In the case of **2**, after 180 °C there are four decomposition steps (figure 1(b)): up to 349 °C (weight loss found 37%), up to 372 °C (weight loss found 40%), up to 439 °C (weight loss found 46%) and up to 547 °C (weight loss found 61%). The main steps of weight loss correspond to the largest exothermic peaks (21% for **1** and 15% for **2**), which are most probably oxidation of organic and carbon residues in the air and a contribution of the exothermic crystallization. Note that due to the strong exothermic reaction, the temperature of a pellet will be significantly higher than that of the kiln, which promotes crystallization. After these

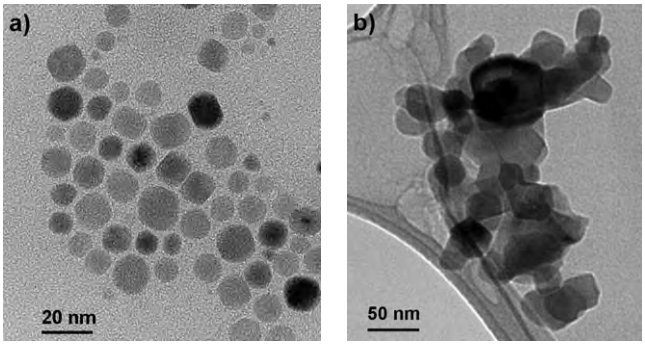

Figure 3. TEM images of as-prepared $Gd_{1.90}Eu_{0.10}O_3$ (a) and $Y_{1.90}Eu_{0.10}O_3$ annealed at 1000 °C (b).

fragmentations, no thermal effects were noticed from DTA curves (figures 1(a) and (b)). The colours of both samples were white after the thermal treatment.

The main differences between thermolysis of **1** and **2** in the synthesis process of $Y_{1.80}Eu_{0.20}O_3$ and $Gd_{1.90}Eu_{0.10}O_3$ were observed from the TGA and DTA curves at higher temperatures up to about 880 °C, where after 547 °C **2** loses only 3.0%, while after 573 °C **1** loses even 7.3% of the weight. Thus the structure of the residue of **2** up to about 500 °C is very close to the final product $Gd_{1.90}Eu_{0.10}O_3$ of the thermolysis. This is in good agreement with the XRPD patterns of **2** (figure 2(b)), when the changes in microstructure to bixbyite type were gradually observed after annealing at 500, 650, 800, and 1000 °C. All reflections in the observed patterns were indexed in the expected space group $Ia\bar{3}$. The reflections correspond to the bixbyite type were already observed after annealing at 500 °C for **2** (figure 2(b)) and intensities are stronger as the annealing temperature is increased.

A similar conclusion about the type of structure obtained by thermolysis of **1** could not be defined after 500 °C because sample **1** did not totally decompose up to about 500 °C (figure 1(a)). XRPD patterns of **1** (figure 2(a)) after annealing at 500 °C also confirm that peaks are not appropriate for the space group $Ia\bar{3}$. After annealing at 1000 °C, sample **1** was crystallized as expected, i.e. XRPD patterns for both compounds (figures 2(a) and (b)) are almost the same and correspond to the bixbyite structures.

The TGA and DTA curves clearly show that the temperature of 880 °C (figures 1(a) and (b)) corresponds to a complete decomposition of both organometallic precursors with the very similar residual masses of about 33 and 36% to give $Y_{1.80}Eu_{0.20}O_3$ and $Gd_{1.90}Eu_{0.10}O_3$, respectively, which were proved to be bixbyites.

3.2. Crystal structure and microstructure

The size and morphology of the nanoparticles constituting our samples were assessed by TEM. In figures 3(a) and (b), TEM images are shown for $Gd_{1.90}Eu_{0.10}O_3$ (as-prepared) and $Y_{1.90}Eu_{0.10}O_3$ (annealed at 1000 °C), respectively. Particles are spherically shaped with facetted morphology, showing some dispersion of particle size around an average value of 8–10 nm. For particles annealed at 650 and 800 °C, the average size of particles increased to ∼12 nm, with a higher fraction of larger particles. It can be noticed that the difference in half widths at half maxima in diffraction patterns of samples annealed at 650 and 800 °C (figure 2(b)), point out the difference in particle size distributions. Comparing this with TEM observations it can be concluded that the particles for two samples are composed from different numbers of crystallites. After annealing at 1000 °C the size of particles increased to ∼30–50 nm. These results are in agreement with the increase of crystallite size with annealing observed from x-ray diffraction patterns (figure 2).

Table 1. Refined values of occupation numbers (Occ) and lattice parameters for samples $Y_{2-x}Eu_xO_3$ ($x = 0.06, 0.10, 0.20$).

Molar ratio x	Occ (C_{3i})	Occ (C_2)	a (Å)
0.06	0.021(12)	0.099(12)	10.6137(1)
0.10	0.038(16)	0.162(16)	10.6174(1)
0.20	0.065(17)	0.335(17)	10.6296(1)

$Y_{2-x}Eu_xO_3$ and $Gd_{2-x}Eu_xO_3$ were found to crystallize in the cubic C-type or bixbyite structure (space group $Ia\bar{3}$), where the cations are distributed over two nonequivalent Wyckoff-positions: 8b with local symmetry C_{3i} and 24d with local symmetry C_2. Oxygen ions are located on the general 48e positions [8]. Cation site occupancy is a very important structural parameter that determines optical, magnetic, and other physical properties. From the optical point of view the C_{3i} site has a centre of inversion and then, according to selection rules, all electric dipole transitions are forbidden. The C_2 site does not have inversion symmetry and electric and magnetic dipole transitions are allowed [9].

To determine C_{3i}/C_2 site occupancies from x-ray diffraction data for $Y_{2-x}Eu_xO_3$, we used the Fullprof program [10]. In the initial stage of refinement we fixed occupancy to random distribution. In the later stages occupation parameters were refined. Obtained values of C_{3i}/C_2 site occupancies of Eu^{3+} are given in table 1. Both site occupancies increase proportionally with increase of Eu^{3+} concentration in the sample. The refined values of lattice parameter are shown in table 1. Lattice parameter $(a), a(x)$ (Å) $= 10.6047(8)$ (Å) $+ 0.1278(8)x$ (Å), linearly increases with increasing concentration. This behaviour is a consequence of different ionic radii of octahedrally coordinated Y^{3+} (104 pm) and Eu^{3+} (108.7 pm), while linearity confirms that the solid solutions were synthesized.

XRPD of $Gd_{2-x}Eu_xO_3$ were used to determine lattice parameters. Obtained values are 10.8152(2) Å and 10.8173(2) Å for $x = 0.06$ and 0.10, respectively. The fact that Eu^{3+} and Gd^{3+} are the 'first neighbours' in the periodic system precludes determination of site occupancies from XRPD.

3.3. Photoluminescence studies

Figure 4 shows the emission spectra of $Y_{2-x}Eu_xO_3$ ($x = 0.06, 0.10, 0.20$) obtained by direct excitation of Eu^{3+} at 390 nm. The spectra between 580 and 700 nm are composed of emission peaks of Eu^{3+} ions that are related to transitions from the excited $^5D_0$ level to ^7F_j ($j = 1$–4) levels. The first

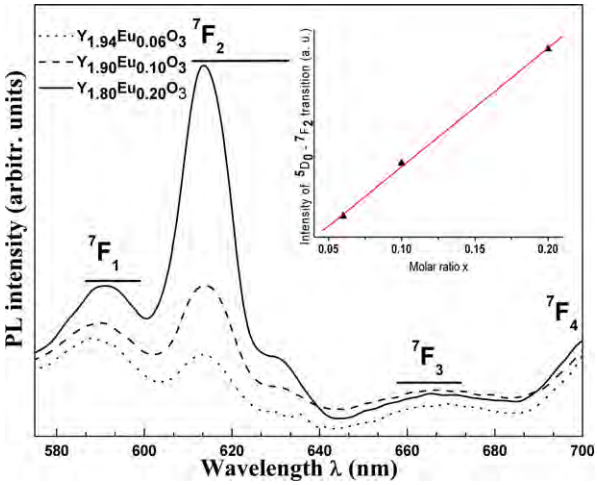

Figure 4. Emission spectra of $Y_{2-x}Eu_xO_3$ samples. The inset: asymmetric ratio versus molar ratio x.

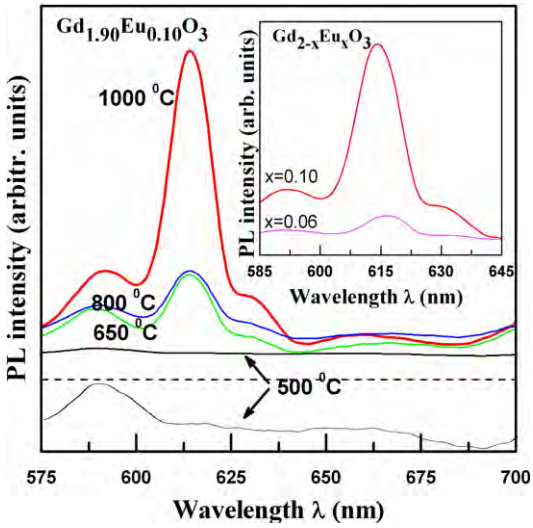

Figure 5. Emission spectra of $Gd_{2-x}Eu_xO_3$ ($x = 0.10$) samples annealed at temperature 500–1000 °C. At the bottom is an enlarged spectra for the sample annealed at 500 °C. The inset: emission spectra of $Gd_{2-x}Eu_xO_3$ ($x = 0.10$ and 0.06) samples annealed at 1000 °C.

peak at approximately 592 nm corresponds to the magnetic dipole transition ($^5D_0$–$^7F_1$), while the second peak centred at 614 nm corresponds to the electric dipole transition ($^5D_0$–$^7F_2$). Regarding the peak position in the spectra, no shift is found when Eu^{3+} concentration is changed. However, a difference in peaks intensity is evident, see figure 4. The biggest PL intensity was observed for the highest Eu^{3+} concentration ($x = 0.20$, shown in the inset) and the smallest for the lowest concentration ($x = 0.06$). PL emission intensity depends both on the concentration of Eu^{3+} ions and their distribution between two crystallographic sites. According to Judd–Ofelt theory [11, 12] the intensity of the $^5D_0$–$^7F_1$ peak does not depend on the local environment, whereas the electric dipole transition $^5D_0$–$^7F_2$ is very sensitive to the symmetry of the cation surroundings. That is, if the europium ions occupy C_2 sites, the $^5D_0$–$^7F_2$ transitions will be dominant, but if the Eu^{3+} occupy sites with inversion symmetry (C_{3i}) the emission corresponding to the $^5D_0$–$^7F_1$ transition will be more pronounced. Since the intensities of both electric and magnetic transition are strong enough, the former allows us to conclude that the distribution of Eu^{3+} is random between C_2 and C_{3i} sites. This result is in accordance with the cation distribution found by the refinement of occupation numbers (section 3.2).

Additional analysis of PL emission spectra was done through the peaks' integrated intensity for $^5D_0$–$^7F_2$ transition. The corresponding spectral lines were fitted with a Gaussian function. The peak intensity versus molar ratio x is inserted in figure 4. It can be seen that the intensity increases linearly with the increase in concentration of active Eu^{3+} ions from 3% ($x = 0.06$) to 10% ($x = 0.20$). It is worth mentioning that some factors have an influence on emission intensity. The increase in Eu^{3+} concentration increases the number of PL active centres (and consequently the PL intensity); higher concentrations of Eu^{3+} ions can lead to non-radiative exchange of the absorbed energy and thus to luminescence quenching [13]. Next, from the magnetic point of view, the solid solutions are magnetically diluted, and for low concentrations there is a tendency of magnetic-ion cluster formation [14]. Consequently, possible clustering of magnetic Eu^{3+} in the samples could influence their emission intensity. The inspection of literature data of Y_2O_3:Eu revealed that the differences in emission intensities depend on cation distributions and concentrations as well as on microstructures of samples. For the $Y_{2-x}Eu_xO_3$ series, Li *et al* reported the maxima in intensity for $x = 0.10$ [15], the same as Kim *et al* [16]. The Y_2O_3:Eu spherical particles synthesized in microemulsions optimized luminescence properties for 10% of Eu [17]. Our results reveal that the PL intensity increases with increasing concentration of Eu^{3+} from 3 up to 10%.

In the case of $Gd_{2-x}Eu_xO_3$ ($x = 0.06, 0.10$) samples the concentration and size dependence of PL emission was studied. Spectra for an as-prepared (at 500 °C) $x = 0.10$ sample (after direct excitation of Eu^{3+} at 390 nm) as well as after thermal annealing at 650, 800, and 1000 °C are presented in the main panel of figure 5. The peaks corresponding to magnetic ($^5D_0$–$^7F_1$) and electric ($^5D_0$–$^7F_2$) allowed transitions to appear at the positions found in the literature for the same phosphor, e.g. [5]. There is no shift in peak position either with annealing or a change in concentration of Eu^{3+}. An interesting observation is that in the as-prepared sample the peak corresponding to electric transition at ∼615 nm is of very low intensity (the bottom of the main panel). Consequently, we can conclude that the distribution of Eu^{3+} active centres depends on particle size, and so in the as-prepared sample the distribution is preferential at C_{3i} sites, while in the annealed sample Eu^{3+} are distributed at sites C_2 and C_{3i}. The intensity of the main peak located at ∼614 nm increases with increasing crystallinity. The concentration dependence on PL emission of $Gd_{2-x}Eu_xO_3$ samples annealed at 1000 °C is presented as an inset in figure 5. It can be seen that the emission intensity is higher for $x = 0.10$ than for $x = 0.06$. In the literature the optimum luminescence was observed for 5–10% of Eu^{3+} in the Gd_2O_3 host [18].

Additional analysis of PL emission spectra was done through the calculated ratio of the peaks' integrated intensity

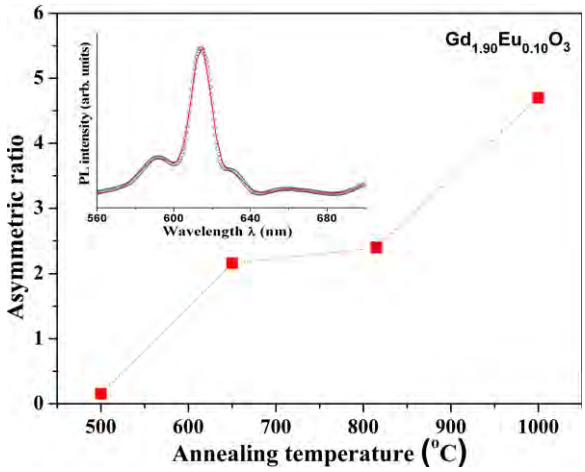

Figure 6. Asymmetric ratio versus annealing temperature for $Gd_{1.90}Eu_{0.10}O_3$. The dashed line is a guide for the eyes. The inset: Gaussian fit of PL spectra for the sample annealed at 1000 °C.

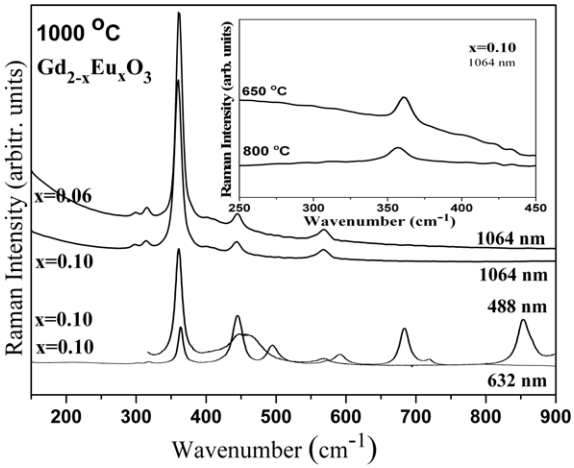

Figure 7. FT-NIR Raman spectra of $Gd_{2-x}Eu_xO_3$ ($x = 0.06$) and FT-NIR Raman and FT Raman (two on the bottom) spectra of $Gd_{2-x}Eu_xO_3$ ($x = 0.10$) obtained using different lasers. The inset: FT-NIR Raman spectra of $Gd_{2-x}Eu_xO_3$ ($x = 0.10$). Corresponding temperatures of sample annealing are given.

for $^5D_0$–$^7F_1$ and $^5D_0$–$^7F_2$ transitions (asymmetric ratio, $A = \int {}^5D_0{-}^7F_2 / \int {}^5D_0{-}^7F_1$). The asymmetric ratio was calculated using the fitting parameters of the Gaussian type profile for the magnetic and electric transition peaks. The dependence of the asymmetric ratio on annealing temperature for $x = 0.10$ is given in figure 6. It can be seen that it increases from 0.15 to 4.4 with the increase in annealing temperature (particle size) from 500 to 1000 °C. The ratio A is considered to be the indicator of the symmetry of the coordination environment around the Eu^{3+} ion and is influenced by cation site occupancies, distortion of the lattice, and the nanophase character of the sample. It should be noted that cation replacement in the samples influences changes in bond distances and angles.

3.4. Raman spectroscopy

The concentration/size effects on Raman spectra of $Y_{2-x}Eu_xO_3$ and $Gd_{2-x}Eu_xO_3$ were studied using various different excitations in order to obtain vibrational spectra without undesired overlapping with the PL electronic transitions. A high-resolution 'XY' spectrograph with excitation of 488 nm (5 mW) and an INFINITY spectrograph with excitation of 632 nm were used. As an example, the spectrum for $Gd_{1.90}Eu_{0.10}O_3$ annealed at 1000 °C shown at the bottom in figure 7 consists of the superposition of the vibrational signature with the stronger PL band peaking at ∼460 cm^{-1}. In the same panel $Gd_{2-x}Eu_xO_3$ spectra obtained by an NIR Raman spectrometer are shown. The low energy of the IR excitation prevents excitations of Eu electronic levels and hence the Raman spectrum is not contaminated by the electronic transitions.

The full width at half maximum (FWHM) of the strongest ∼360 cm^{-1} peak for $Gd_{1.90}Eu_{0.10}O_3$ decreases with the particle size increase as follows: it is 14.5 cm^{-1} for the sample annealed 1 min at 800 °C, ∼12 cm^{-1} for the sample annealed 2 h at 650 °C, and ∼11 cm^{-1} for the sample annealed 72 h at 1000 °C. The FWHM for the sample with $x = 0.06$ annealed at 1000 °C was found to be slightly lower yet, namely

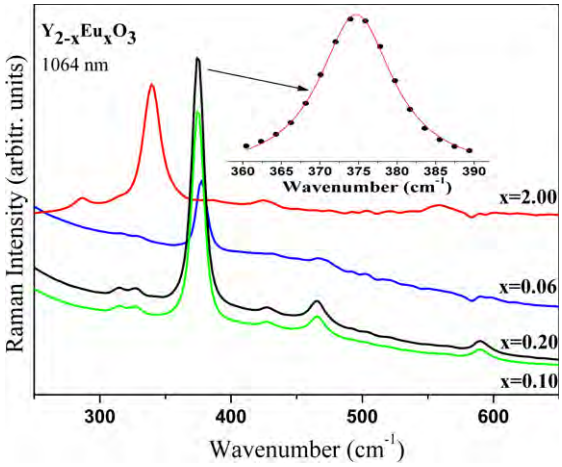

Figure 8. FT-NIR Raman spectra of $Y_{2-x}Eu_xO_3$ ($x = 0.06, 0.10, 0.20, 2.00$) samples annealed at 1000 °C. The inset: Lorentzian fit of the 365 cm^{-1} mode for $x = 0.20$ sample.

∼10 cm^{-1}. Concerning evolution of the bands' position with annealing, the strongest peak is found to be slightly shifted toward higher frequencies. It should be noted that band broadening is intrinsic to many nanophased oxides, as both small particle size and defects (substitution vacancies) hinder regular phonon propagation and hence induce Brillouin zone folding which makes all phonons Raman active [19–23]. Additionally, inspection of the literature data indicates that in the rare earth sesquioxides Raman band broadening increases as the ionic radius of the rare earth atom is increasing [24]. Accordingly, results for FWHM in Eu_2O_3 and Eu substituted Gd_2O_3 are consequences of both the nanophase character of the samples and partial cation substitution.

The Raman spectra of $Y_{2-x}Eu_xO_3$ ($x = 0.06, 0.10, 0.20$) after excitation with 1064 nm are presented in figure 8. The inset shows an example of the best fit for the $x = 0.2$ composition obtained using one Lorentzian peak as

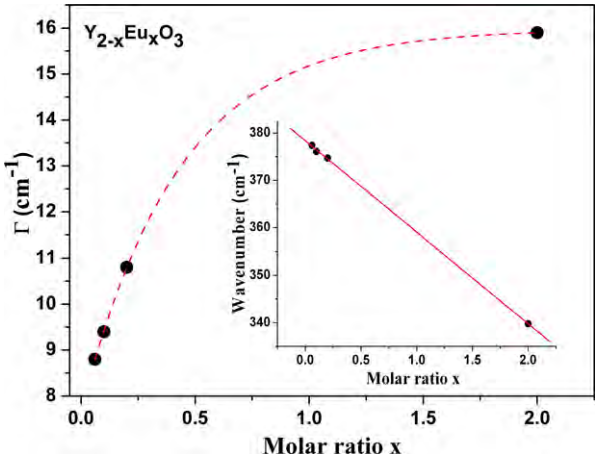

Figure 9. The change of the bandwidth and position (the inset) of the most intense Raman mode of $Y_{2-x}Eu_xO_3$ versus molar ratio x (the dot–dot line is a guide for the eyes).

expected. All observed bands correspond to the structure model described within space group $Ia\bar{3}$. As in the case of $Gd_{2-x}Eu_xO_3$, additional bands due to electronic transitions appeared in the spectra upon excitations with 488 and 632 nm (not shown). From the fitting parameters for the strongest mode at about 365 cm^{-1}, based on the Lorentzian type profile, we were able to get information about the changes in position and bandwidth due to changes in Eu^{3+} concentration. This change of bandwidth is presented in figure 9, while the inset shows the position of the strongest mode versus Eu^{3+} concentration. Position of the bands is systematically shifted toward higher frequencies with increasing molecular mass, from 347 cm^{-1} for Eu_2O_3 to 381 cm^{-1} for the sample with $x = 0.06$. The main peak wavenumber changes linearly with the substitution level, confirming the formation of a solid solution on a very local scale of the Raman probe. Thus Raman microspectrometry can be efficiently used to control the composition of the material. The topological resolution (up to 1–5 μm as a function of excitation wavelength and optics) allows inspection of the homogeneity at the micrometre scale.

4. Conclusion

A synthesis route for the preparation of red emitting $Y_{2-x}Eu_xO_3$ ($x = 0.06, 0.10, 0.20$) and $Gd_{2-x}Eu_xO_3$ ($x = 0.06, 0.10$) phosphors by thermal decomposition of 2,4-pentanedione complexes was reported in this paper. Analysis of the thermal decomposition process was done by TGA/DTA and XRPD measurements. While after thermal treatment at 500 °C a bixbyite structure of $Gd_{2-x}Eu_xO_3$ was formed, the formation of the bixbyite phase of $Y_{2-x}Eu_xO_3$ required higher temperature. The reported method enables the formation of nanopowders with spherical particles with sizes of 8–10 nm. Dependence on lattice parameter, crystallographic distribution, PL intensity, Raman peak position, and FWHM on Eu^{3+} concentration, was studied. The Eu^{3+} ions in host Y_2O_3 and Gd_2O_3 occupy C_2 and C_{3i} sites after sample annealing, while Eu^{3+} have preference for C_{3i} sites in the as-prepared $Gd_{1.90}Eu_{0.10}O_3$ sample. It seems that a metastable distribution (preference of Eu^{3+} toward C_{3i} sites) exists in nanoparticles and distribution becomes random upon thermal annealing. The luminescence intensities are size dependent, and increase as the size (degree of crystallinity) increases. The PL intensity shows that the quenching concentration of Eu^{3+} ions in the investigated host matrices is above 10%.

Acknowledgments

This work has been financially supported by both the Serbian Ministry of Science and Technology and SCOPES project (grant No. IZ73Z0_1 27961).

References

[1] Nelson J A, Brant E L and Wagner M J 2003 *Chem. Mater.* **15** 688
[2] Yoo H S, Yang H S, Im W B, Kang J H and Jeon D Y 2007 *J. Mater. Res.* **22** 2017 and references therein
[3] Bae Y J, Lee K H and Byeon S H 2009 *J. Lumin.* **129** 81
[4] Devaraju M K, Yin S and Sato T 2009 *J. Cryst. Growth* **311** 580
[5] Mahajan S V and Dickerson J H 2007 *Nanotechnology* **18** 325605
[6] Blanusa J, Antic B, Kremenovic A, Nikolic A S, Mazzerolles L, Mentus S and Spasojevic V 2007 *Solid State Commun.* **144** 310
[7] Kremenovic A, Antic B, Nikolic A S, Blanusa J, Meden T and Jancar B 2007 *Scr. Mater.* **57** 1061
[8] Marezio M 1966 *Acta Crystallogr.* **20** 723
[9] Vetrone F, Boyer J C, Capobianco J A, Speghini A and Bettinelli M 2003 *Chem. Mater.* **15** 2737
[10] Rodriguez-Carvajal J 2010 *FullProf Comp. Program* http://www.ill.eu/sites/fullprof/php/downloads.html
[11] Judd B R 1962 *Phys. Rev.* **127** 750
[12] Ofelt G S 1962 *J. Chem. Phys.* **37** 511
[13] Ferrari J L, Pires A M and Davolos M R 2009 *Mater. Chem. Phys.* **113** 587
[14] Antic B, Mitric M, Rodic D, Zhong Y, Artemov Y, Bogdanovich S and Friedman J R 1998 *Phys. Rev.* B **58** 3212
[15] Li J-G, Li X, Sun X and Ishigaki T 2008 *J. Phys. Chem.* C **112** 11707
[16] Kim E J, Kang Y C, Park H D and Ryu S K 2003 *Mater. Res. Bull.* **38** 515
[17] Huang H, Xu G Q, Chin W S, Gan L M and Chew C H 2002 *Nanotechnology* **13** 318
[18] Ningthoujam R S, Shukla R, Vatsa R K, Duppel V, Kienle L and Tyagi A K 2009 *J. Appl. Phys.* **105** 084304
[19] Kremenovic A, Blanusa J, Antic B, Colomban Ph, Kahlenberg V, Jovalekic C and Dukic J 2007 *Nanotechnology* **18** 145616
[20] Gouadec G and Colomban Ph 2007 *Prog. Cryst. Growth Charact. Mater.* **53** 1
[21] Colomban P 2004 *Mater. Sci. Forum* **453/454** 269
[22] Colomban P 2003 *Spectrosc. Eur.* **15** 8–16
[23] Kosacki I, Suzuki T, Anderson H U and Colomban P 2002 *Solid State Ion.* **149** 99–105
[24] Panitz J C 1999 *J. Raman Spectrosc.* **30** 1035